Mesoporous Carbon−Carbon Nanotube−Sulfur Composite Microspheres for High-Areal-Capacity Lithium−Sulfur Battery Cathodes

Terrence Xu,[‡] Jiangxuan Song,[‡] Mikhail L. Gordin, Hiesang Sohn, Zhaoxin Yu, Shuru Chen, and Donghai Wang*

Department of Mechanical and Nuclear Engineering, The Pennsylvania State University, University Park, Pennsylvania 16802, United States

Ⓢ *Supporting Information*

ABSTRACT: Lithium−sulfur (Li−S) batteries offer theoretical energy density much higher than that of lithium-ion batteries, but their development faces significant challenges. Mesoporous carbon−sulfur composite microspheres are successfully synthesized by combining emulsion polymerization and the evaporation-induced self-assembly (EISA) process. Such materials not only exhibit high sulfur-specific capacity and excellent retention as Li−S cathodes but also afford much improved tap density, sulfur content, and areal

capacity necessary for practical development of high-energy-density Li−S batteries. In addition, when incorporated with carbon nanotubes (CNTs) to form mesoporous carbon−CNT−sulfur composite microspheres, the material demonstrated superb battery performance even at a high current density of 2.8 mA/cm^2, with a reversible capacity over 700 mAh/g after 200 cycles.

KEYWORDS: *areal capacity, lithium−sulfur batteries, microspheres, porous carbon, sulfur loading*
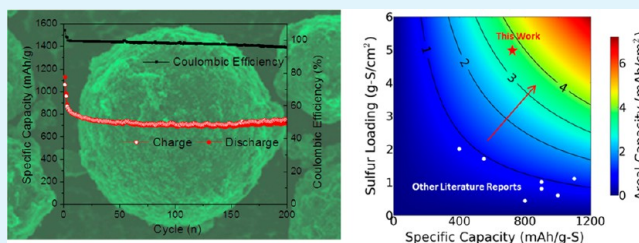
1. INTRODUCTION

Lithium−sulfur (Li−S) batteries have been fervently pursued as a next-generation energy storage system due to their high theoretical energy density and projected low cost compared with lithium-ion batteries (LIBs). Li−S batteries operate by reaction of sulfur with lithium to form lithium polysulfides (i.e., Li_2S_x, $8 \geq x \geq 3$), lithium disulfide (Li_2S_2), and finally lithium sulfide (Li_2S) during the lithiation process, with the reverse occurring during the delithiation process. Calculated based on sulfur, Li−S batteries have a high theoretical energy density of 2600 Wh/kg and a high specific capacity of 1672 mAh/g.[1,2] Despite these promising traits, there exist fundamental challenges to utilizing Li−S batteries for practical applications. These mainly stem from two factors. First, both sulfur and its final lithiation product, Li_2S, are highly electronically and ionically insulating. The kinetics of electrochemical lithiation of sulfur and delithiation of Li_2S are thus slow, which results in a low attainable capacity.[3,4] Second, lithium polysulfides readily dissolve in the electrolyte. This dissolution causes a series of problems, including loss of cathode materials by diffusion away from the cathode, collapse of the cathode structure, and the polysulfide shuttle effect.[3,5−9] As a result, Li−S batteries commonly show fast capacity decay and low Coulombic efficiency. Diverse approaches have been explored to address these; in particular, nanostructured carbon−sulfur composites have been proved to successfully increase and stabilize the achievable capacity.[10−14] Well-designed porous carbon frameworks can confine sulfur particles at the nanoscale, serving to

address both of the core challenges of Li−S batteries. Such frameworks provide a highly conducting network for electron transfer, thus enabling a faster lithiation/delithiation process and improving sulfur utilization. In addition, their high surface area can trap polysulfides in the cathode through physical adsorption and thus improve capacity retention during cycling. The surface chemistry of the carbon framework can further be tuned by hetero-atom doping, for enhanced adsorption of sulfur species and consequently improved battery performance.[15] This approach evidently expanded the design dimension and versatility of carbon−sulfur composites as promising cathode materials for Li−S batteries.

Besides sulfur-specific capacity and capacity retention, several other factors are also critical for the development of high-energy Li−S batteries but have received little attention in the literature—in particular, these include (1) tap density of cathode materials, (2) sulfur content in cathode materials, and (3) sulfur loading of electrodes. First, the tap density of a cathode material plays a key role in determining its volumetric capacity—a higher tap density indicates denser packing of the cathode material and thus higher volumetric capacity.[16] Much of the work to date on sulfur cathodes has focused on cathode materials with sub-micrometer-sized or nanosized particles; however, it is well known that such small particles generally
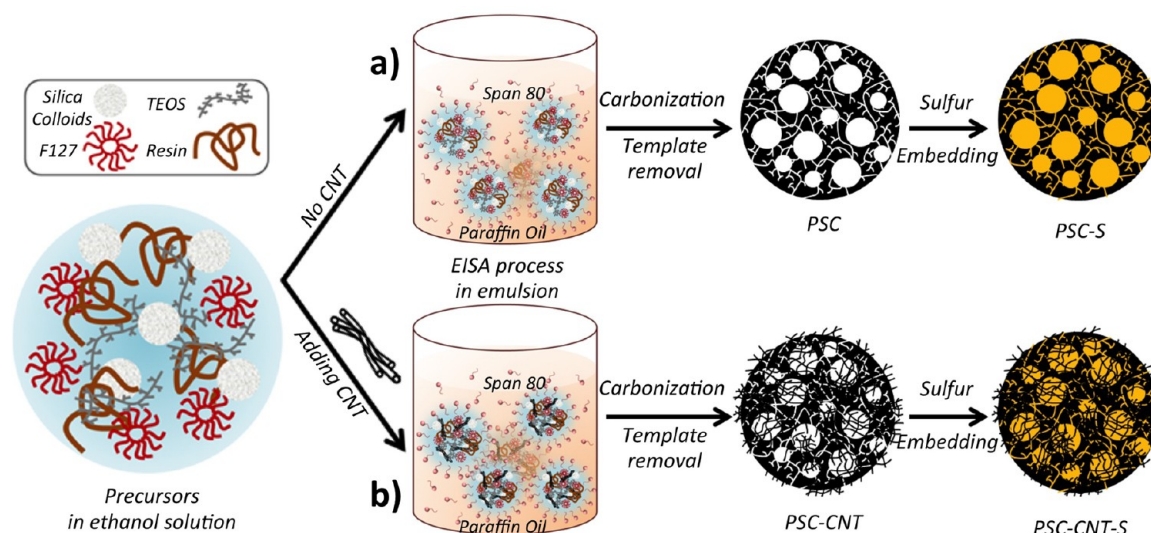
Figure 1. Schematic illustration for the synthesis of (a) PSC−S and (b) PSC−CNT−S using a combination of the emulsion polymerization process and the EISA method.

exhibit a relatively low tap density. Second, sulfur content (mass fraction of sulfur in cathode materials) affects the specific capacity of the cathode material as a whole, which is simply the multiplication product of sulfur-specific capacity and sulfur content. However, increasing the sulfur content can make it difficult to maintain good overall ionic and electrical conductivities or to suppress the polysulfide shuttle, leading to decreased sulfur-specific capacity and poorer cycling stability and rate performance.[17] Finally, sulfur loading of electrodes (amount of sulfur coated on electrodes) determines the total capacity per electrode and consequently the energy density of a battery. Electrodes with high sulfur loading—and thus with high capacity—are required for fabricating high-energy density batteries, as they decrease the relative content of inactive components in the battery, such as current collectors and membranes.[18−20] Assuming a discharge voltage of 2 V and specific capacity of 800 mAh/g for Li−S cathodes, a sulfur loading of 5 mg S/cm^2 is necessary to get an energy density comparable with that of cathodes in commercial LIBs (see calculation in Supporting Information). However, achieving such a high sulfur loading in electrodes is difficult with conventional Li−S cathode materials, as their submicrometer-sized or nanosized particles lead to severe cracking of the electrode with increased loading; previous publications mostly reported electrode loadings of only 1−2 mg S/cm^2 when using industry-adopted coating techniques.[11,13,21−25] In addition, high loading can lead to increased electrical and ionic resistance and thus poor rate performance.[17] These three parameters need to be optimized, but raising each can be detrimental to capacity and rate performance. The key to balancing these competing parameters is the design of high-performance, well-optimized cathode materials.

Microsized materials have favorable properties in Li−S battery applications compared with submicrometer-sized or nanosized materials. Such materials generally possess a higher tap density, granting them higher volumetric energy density. They also have a lower number of particle−particle interfaces, often leading to a lower contact resistance and easier-to-bind electrodes. Combining these advantages of microsized materials with the aforementioned advantages of nanostructured carbon−sulfur composites, here we report the design of a

carbon framework that possesses both microsized spherical particle morphology and hierarchical mesopores to form a porous spherical carbon−sulfur composite (PSC−S). Both microscale particle morphology and pore structure in the porous spherical carbon (PSC) were well controlled by combining emulsion polymerization and the evaporation-induced self-assembly (EISA) process. The PSC−S composite boasts a high tap density of 1.08 g/mL and contains 75 wt % sulfur embedded into the mesopores of its carbon framework. At a high sulfur loading of 5 mg S/cm^2 and 60 wt % sulfur content in the electrode, this material delivers both high gravimetric and high volumetric capacity with excellent retention. Carbon nanotubes (CNTs) can also be readily incorporated into the microspherical structure in the synthesis process to form a porous spherical carbon−carbon nanotube−sulfur composite (PSC−CNT−S). CNT incorporation effectively raises the conductivity of the composite and thus significantly improves its high rate performance. At a high current density of 2.8 mA/cm^2, an initial capacity of 1100 mAh/g and a reversible capacity of 700 mAh/g after 200 cycles were achieved in PSC−CNT−S. The resultant areal capacity of over 3.5 mAh/cm^2 is much higher than in previous reports of Li−S cathodes fabricated using coating techniques.

2. RESULTS AND DISCUSSION

The synthesis process of microsized PSC−S spheres is schematically illustrated in Figure 1a. To simultaneously control both the microscale morphology and mesoporous structure, a combined process of emulsion polymerization and EISA was adopted.[26−29] The emulsion polymerization process is known to facilitate formation of microspherical particles, while EISA can assemble building blocks of the framework precursor and pore templates into homogeneous mesostructures through a facile solvent evaporation process. Briefly, the carbon precursor (phenolic formaldehyde resin) and several pore templates, namely, tetraethyl orthosilicate (TEOS), triblock copolymer Pluronic F127 (F127), and silica colloids, were homogeneously mixed in ethanol. The aforementioned precursor solution was emulsified in mineral oil by the emulsifier Span 80 under constant mechanical stirring. The emulsion was then heated to
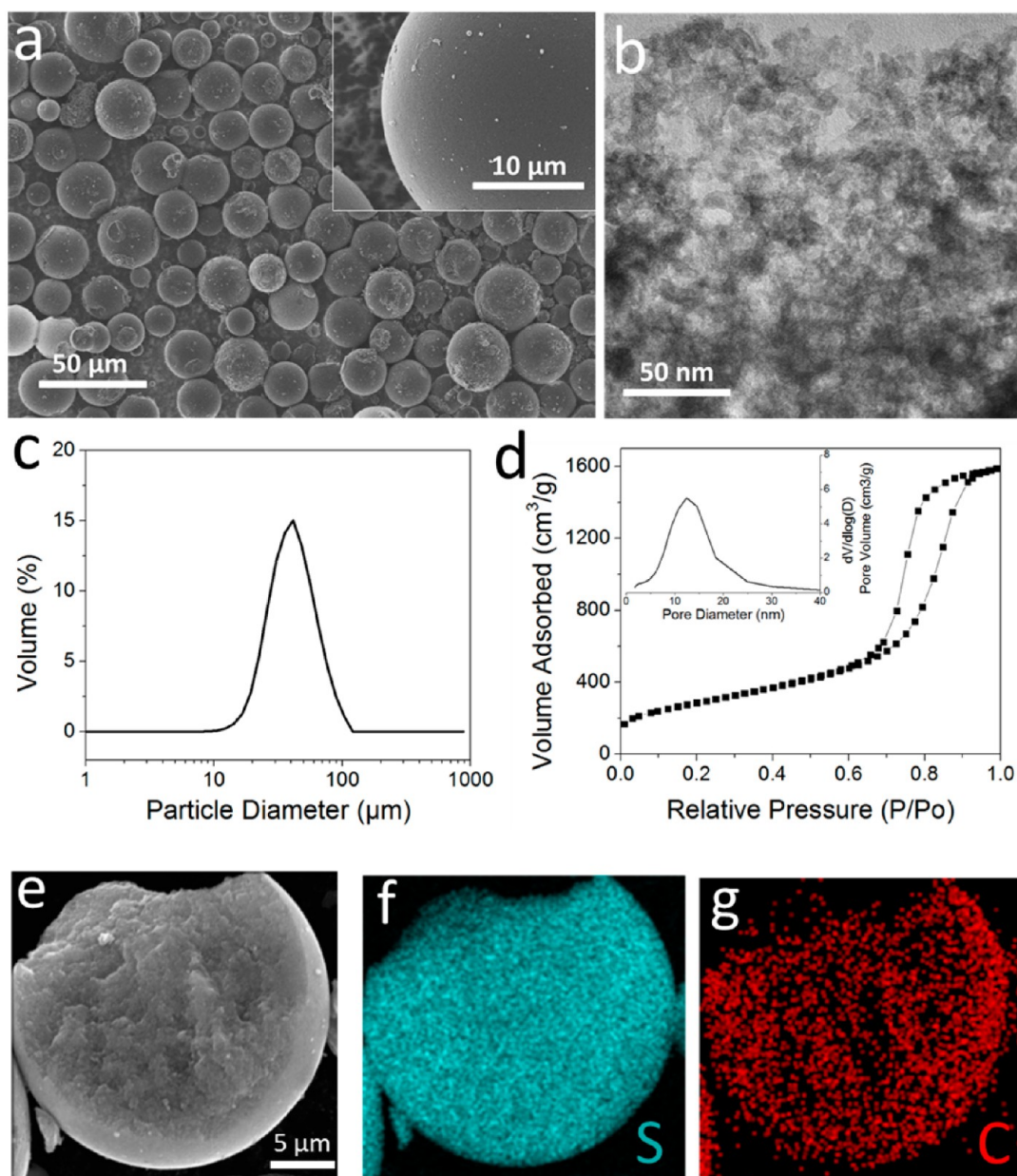
Figure 2. (a) SEM of PSC carbon microspheres; (b) TEM of PSC; (c) DLS measurement on PSC after dispersing particles in water; (d) N₂ sorption isotherms of PSC with inset showing pore size distributions; (e) SEM image of a broken PSC−S composite sphere and its corresponding EDX elemental mapping images of (f) sulfur and (g) carbon.
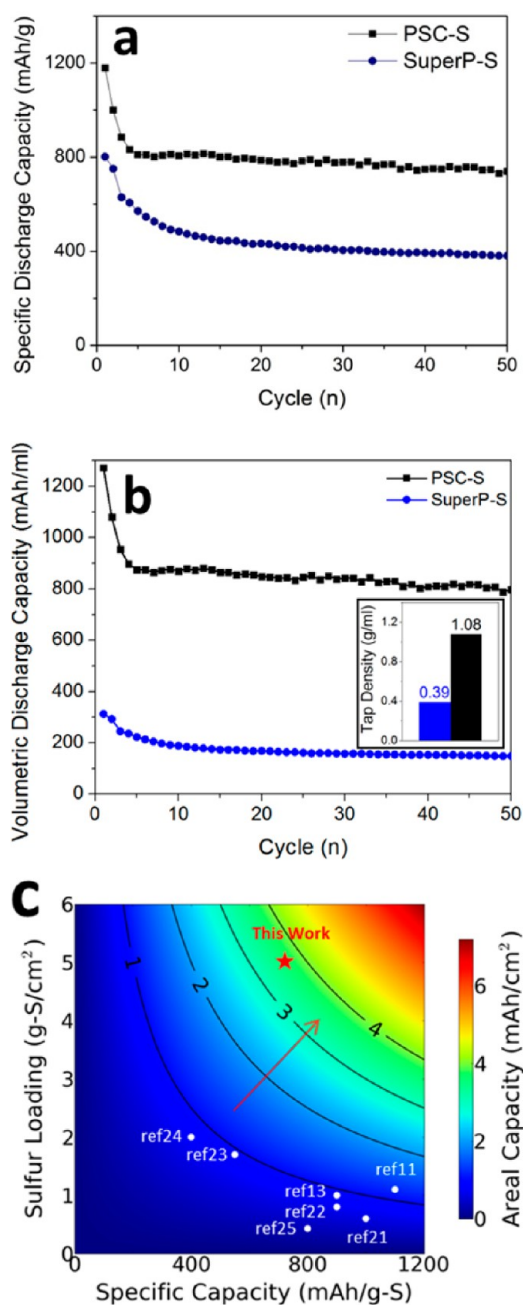
100 °C to allow ethanol evaporation and further polymerization of the resin. As the precursor concentration increased, the emulsion droplets underwent an EISA process to form microsized spheres containing self-assembled mesostructured building blocks. In the EISA process within the droplets, TEOS underwent hydrolysis and the condensation process to form silicate. The silicate, F127, and silica colloids co-directed self-assembly of the resin oligomer into mesostructures via hydrogen bonding.[29] The use of multiple pore templates is to generate hierarchical mesoporous structures with both high surface area (to increase electrochemically active site and polysulfide adsorption) and high pore volume (to increase available space for sulfur embedding). Meanwhile, the emulsifier Span 80 can prevent aggregation of these microsized droplets during thermal polymerization and thus preserve their microspherical morphology. After carbonization and removal of

templates, the hierarchical mesoporous carbon microspheres were obtained and denoted as PSC.

The microscale morphology of PSC particles was studied by scanning electron microscopy (SEM). SEM images confirm that PSC takes the form of microsized spheres (Figure 2a). These spheres have smooth surfaces and diameters in a few tens of micrometers. The volume median diameter of PSC particles was further confirmed by dynamic light scattering (DLS) to be approximately 37 μm (Figure 2c), with the 10th and the 90th percentile at 22 and 63 μm, respectively. The microscale particle sizes of these materials are very suitable for fabricating electrodes with high loading. On the other hand, ball-milling the PSC microspheres may result in shattered particles with irregular shapes and a much reduced diameter (Figure S1, Supporting Information). These particles resemble

those synthesized without morphology control and may yield poor electrode quality when used as electrode materials.

The nanostructure of PSC was investigated by transmission electron microscopy (TEM) and N_2 sorption analysis. The TEM image (Figure 2b) reveals that PSC has a disordered porous structure. Its nitrogen sorption isotherm (Figure 2d) resembles a typical Type IV isotherm with H1 hysteresis, indicating mesoporous structure. The Barrett−Joyner−Halenda (BJH) pore size distribution (Figure 3d) derived from N_2 adsorption shows a peak around 12 nm, with the majority of the mesopores ranging from 5 to 25 nm in diameter. It is

known that the pore size is determined by the employed templates, including silica colloids (10−20 nm), the F127 micelle (4−8 nm), and silica from hydrolyzation and condensation of TEOS (<3.5 nm).[29] This BJH pore size distribution indicates that the majority of mesopores is templated from silica colloids and F127. On the other hand, TEOS templates smaller mesopores in the carbon wall, which generates high surface area and prevents framework shrinkage during the carbonization process. PSC has a high Brunauer−Emmet−Teller (BET) surface area of 1014 m^2/g and a high BJH pore volume of 2.5 cm^3/g, which are critical to battery performance.

Sulfur was then embedded into PSC with a solvent diffusion method to form the PSC−S composite.[30] Sulfur content in the composite was controlled at 75 wt % and confirmed by thermogravimetric analysis (TGA) (Figure S2, Supporting Information). To visually probe the sulfur dispersion in the microsized carbon framework, energy-dispersive X-ray spectroscopy (EDX) was employed to map the distrubution of sulfur, as well as carbon, at a cross-section of a broken PSC sphere (Figure 2e, 2f, and 2g). No noticeable change in the strength of the sulfur signal was observed along the radial direction, indicating that sulfur was uniformly dispersed in PSC spheres. Nitrogen sorption measurements of the composite (Figure S3, Supporting Information) show the slump in pore volume after sulfur embedding, with a remaining BJH pore volume of just 0.06 cm^3/g. This result confirms that sulfur occupied the majority of pores in the carbon framework. However, the remaining porosity should still allow electrochemical reactions to happen smoothly. The X-ray diffraction (XRD) pattern of the composite (Figure S4, Supporting Information) shows no pronounced peaks associated with bulk sulfur, further indicating that sulfur is confined into the mesopores of the carbon frameworks. Owing to its microsized spherical shape in design, PSC−S exhibits an extremely high tap density of 1.08 g/mL, compared with the intrinsic density of ~2.0 g/mL for both amorphous carbon and sulfur (Table 1).

Figure 3. Comparison of cycling performance between PSC−S and SuperP−S at 0.84 mA/cm^2 read in (a) specific discharge capacity and (b) volumetric discharge capacity with the inset showing tap density of the two materials. (c) Comparison of areal capacity in this work with those in the references at the 50th cycle (or the last cycle if cycling ended before the 50th cycle).

Table 1. Tap Densities (g/mL) of Different Carbon−Sulfur Composite Materials

	PSC−S	PSC−bm−S	SuperP−S	PSC−CNT−S
tap density	1.08	0.72	0.39	0.80

The corresponding particle packing efficiency is ~54%, approaching the efficiency of 74% for close packing of monosized spheres and 64% for random close packing of monosized spheres.[31] This discrepency in packing efficiency between the achieved and theoretical value can be attributed to the size variation, the porous structure, and the relatively loose packing of particles. In contrast, by breaking down PSC−S into much smaller and irregular pieces, PSC−bm−S showed a tremendous drop in tap density to 0.72 g/mL. The Super P−sulfur composite (SuperP−S), prepared by mixing commercial carbon Super P and sulfur with the same sulfur content, has an even lower tap density of 0.39 g/mL. A higher tap denisty of battery material is desired for higher volumetric energy density.

PSC−S was evaluated as a cathode material for Li−S batteries by galvanostatic charging/discharging in a coin-cell configuration with lithium metal as the anode. The electrodes were fabricated by doctor blade coating using the C−S composite, Super P, and a PVDF binder with a ratio of 80:12:8. The sulfur content in the cathode was thus 60 wt %.
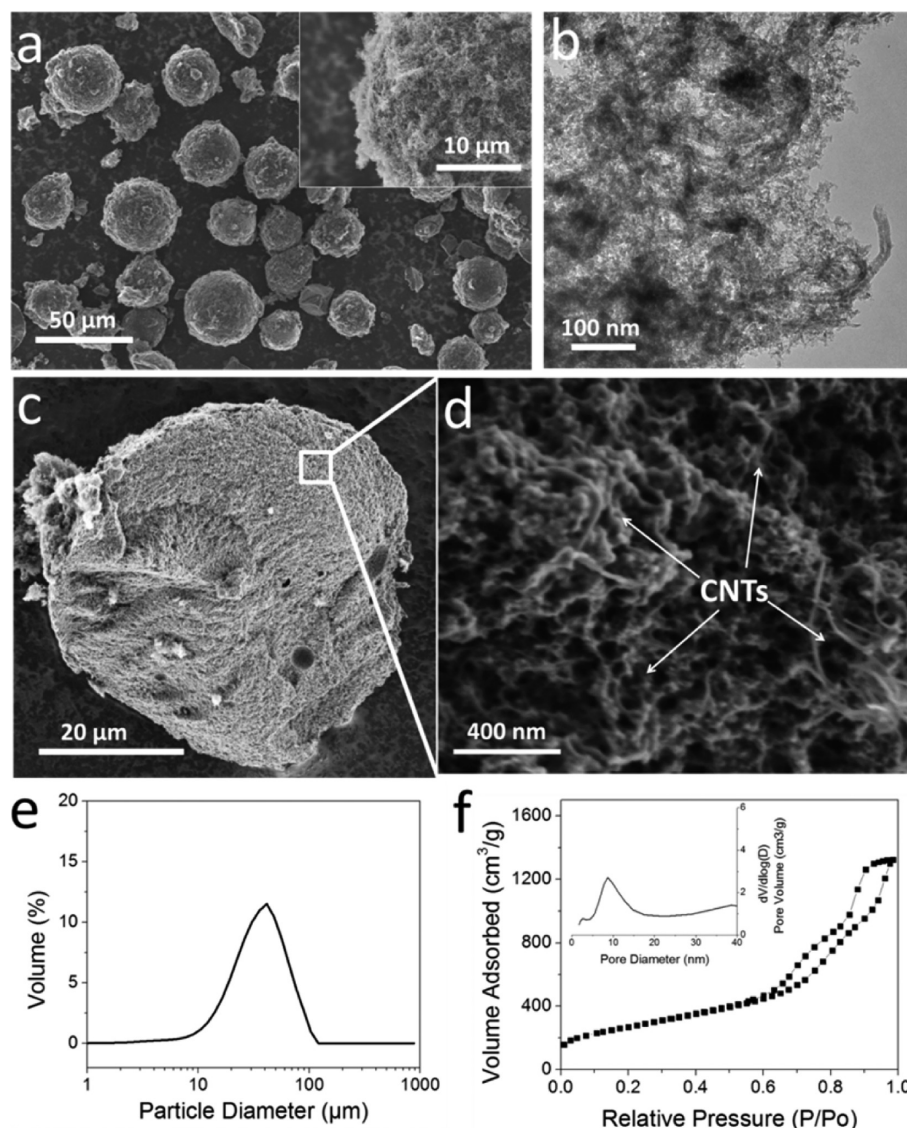
Figure 4. (a) SEM of PSC−CNT microspheres. Inset shows a high-magnification image on the CNT protruding rough surface of the PSC−CNT microspheres. (b) TEM of PSC−CNT. (c) and (d) SEM of the cross-section on a fractured PSC−CNT microsphere. (e) DLS measurement of PSC−CNT after dispersing particles in water. (f) N_2 sorption isotherms of PSC−CNT with inset showing pore size distributions.

The thickness of the electrodes was carefully controlled to get an electrode loading of around 5 mg S/cm^2. SuperP−S electrodes with the same sulfur content and electrode loading were used as control samples. The coating quality of electrodes was shown in Figure S5 (Supporting Information). Because of the ideal particle sizes and high tap density of PSC−S material, its resultant electrode was very smooth and visually crack-free. On the other hand, the PSC−bm−S electrode showed severe cracking due to the significant decrease in particle sizes and tap density. The SuperP−S electrode showed even worse cracking and visible peeling. Electrodes with poor coating quality like the latter two are not viable for battery fabrication, as loose particles may easily come off of the current collector and form short circuits in a cell structure and fail the battery.

Electrodes of the PSC−S composite delivered an initial sulfur-specific discharge capacity of ~1150 mAh/g during activation using a low current density of 0.42 mA/cm^2 (Figure 3a). This initial capacity is close to 70% of the theoretical capacity, showing high utilization of sulfur, likely owing to the intimate contact between nanosized sulfur particles and the mesoporous carbon framework. Cycling continued at 0.84 mA/cm^2 after the initial two activation cycles, and the capacity of PSC−S stabilized at around 800 mAh/g within the subsequent three cycles. A reversible capacity of 740 mAh/g was still delivered after 50 cycles, showing ~91% capacity retention after the first stable cycle, an average drop of 0.20% per cycle. The major capacity drop in the first 5 cycles, a behavior commonly observed in Li−S batteries, may be due to diffusion loss of sulfur species and irreversible formation of Li_2S. It is recognized that increased sulfur loading generally leads to significantly decreased specific capacity.[17] The capacity of the PSC−S composite electrodes is thus impressively high given their high sulfur loading. The high reversible capacity can be attributed to the synergetic effect of several features of PSC−S, namely, its high surface area for polysulfide adsorption, intimate contact between carbon and sulfur, and better mechanical integrity of the electrode that prevents structural collapse due to its microsized, rigid framework. In contrast, SuperP−S delivered much lower capacity and showed fast capacity fading, due to its large sulfur particle size, ease of polysulfide diffusion loss, and

loose framework. Moreover, calculated as the multiplication product of tap density and gravimetric capacity, the volumetric capacity of PSC−S is much higher than that of SuperP−S because of their difference in tap density (Figure 3b).[32,33] At the end of 50 cycles, PSC−S outperformed SuperP−S in volumetric capacity by a factor of 5.

As previously discussed, electrode loading has a significant impact on the energy density of a battery, as higher-loading electrodes mean a lower content of inactive components (such as current collectors and separators) needed for a target cell-level energy density. Previous reports have often used low electrode loading (<2 mg S/cm^2) when using industry-adopted coating techniques, whereas we have determined that an electrode loading of at least 5 mg S/cm^2 (i.e., an areal capacity of 4 mAh/cm^2 assuming 800 mAh/g specific capacity) is necessary to achieve energy density similar to LIB cathodes at the electrode level. Plotted in Figure 3c, the resultant areal capacity of PSC−S at the 50th cycle is much higher than that of previous reports and close to our target value at 4 mAh/cm^2.

High electrical resistance of the sulfur cathodes has long been attributed to limiting sulfur utilization and rate performance of Li−S batteries.[34,35] It gets even more challenging to maintain facile electron transfer with an increased sulfur loading in electrodes. Thus, we leveraged another strength of this synthesis approach, the easiness to incorporate additives into the carbon−sulfur composite, to decrease the electrical resistivity of the material and improve the rate performance of battery. CNTs were illustratively added to the system as conductivity enhancers to form PSC−CNT and PSC−CNT−S, with the latter showing much improved battery performance at high current densities compared with its CNT-free counterpart. PSC−CNT was synthesized similar to PSC, with the additional step of dispersing CNTs in the ethanol precursor solution by sonication and surfactant (Figure 1b, details in Experimental Section). The mass fraction of CNTs in PSC−CNT is estimated to be ∼10%. SEM confirmed the microsized spherical morphology of PSC−CNT (Figure 4a). The particles have rougher surfaces and numerous protruding CNTs (inset in Figure 4a). In addition, CNTs are well dispersed in the interior of the PSC−CNT particles (Figure 4c and 4d). Such a distribution of the conductive CNTs is highly desired to decrease both interparticle and intraparticle electrical resistance and improve the electrode-level conductivity. The size distribution of PSC−CNT particles confirmed by DLS (Figure 4e) is similar to that of PSC, with the volume median diameter to be 33 μm. TEM images (Figure 4b) reveal a disordered mesoporous structure of PSC−CNT. CNTs can be found closely connected with the carbon framework in PSC−CNT. Nitrogen sorption measurements confirmed its mesoporous structure with a Type IV isotherm (Figure 4f). The BJH pore size distribution plot for PSC−CNT shows a peak around 9 nm, followed by a tail contributed by pores with larger sizes. The peak should represent pores templated by F127 and silica colloids, while the tail may represent some pore structures generated by the CNT network (visible in Figure 4d) or aggregated templates. The BET surface area is 963 m^2/g, and the BJH pore volume is 2.1 cm^3/g for PSC−CNT. Both are slightly lower than those of PSC, mostly due to the ∼10 wt % CNT content that has little pore structure. The PSC−CNT porous framework can also hold 75 wt % sulfur in its nanosized pores (Figures S3 and S4, Supporting Information). The tap density of PSC−CNT−S is 0.80 g/mL, lower than that of

PSC−S, which may be due to a looser structure with CNTs in the composite.

The electrical resistivity was measured at different pressures for PSC and PSC−CNT, both before and after sulfur embedding (Figure 5a). For all materials, the resistivity
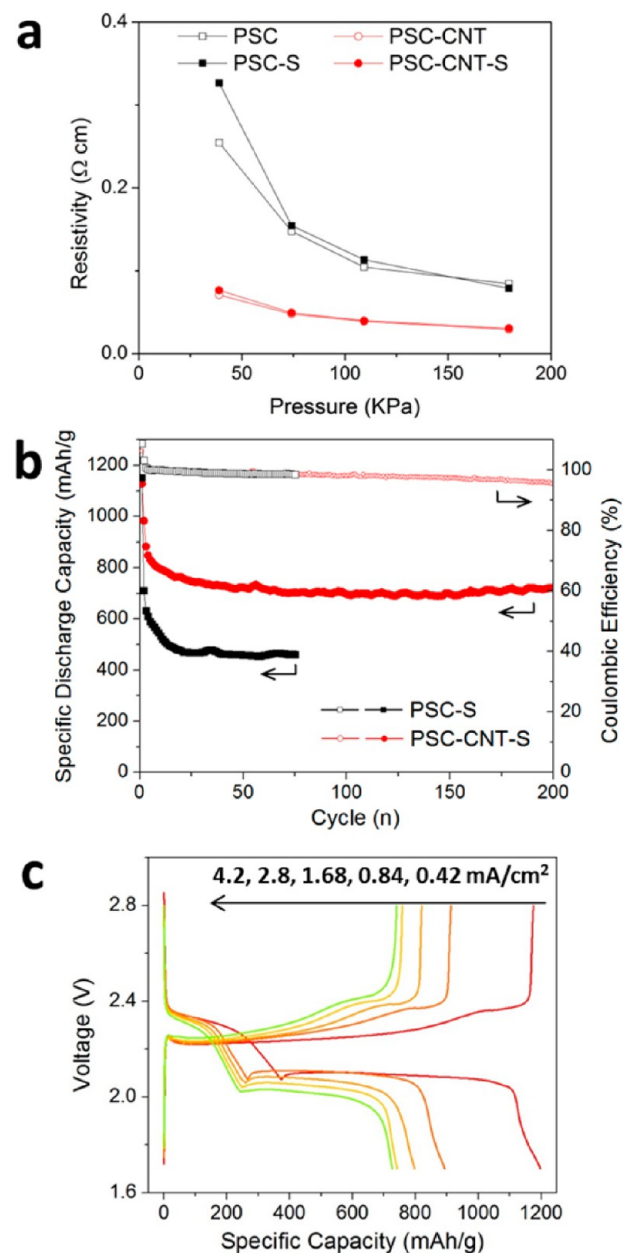
Figure 5. (a) Electrical resistivity measured at various pressures. (b) Comparison of cycling performance between PSC−CNT−S and PSC−S at 2.8 mA/cm^2 with solid dots showing specific discharge capacity and hollow dots showing Coulombic efficiency. (c) Charge−discharge profiles of PSC−CNT−S at various current densities.

decreases with pressure as interparticle contact improves. CNT incorporation causes a clear decrease in resistivity at all testing pressures. It is worth noting that neither PSC nor PSC−CNT exhibited a jump in resistivity after sulfur embedding. This indicates that sulfur is well confined in the pores instead of covering the outer surfaces of the particles, which would otherwise significantly increase contact resistance. This low sensibility of resistivity to sulfur embedding, as well as the

resistivity values of these materials, are consistent with a previous report.[11] PSC−CNT−S showed excellent battery performance at high current densities. As shown in Figure 5b, PSC−CNT−S exhibited stable cycling over 200 cycles at 2.8 mA/cm², which is an extremely high current density in battery applications.[17,36−38] (Note that the first two cycles are acivation cycles at 0.42 mA/cm².) The capacity remained above 700 mAh/g, showing ∼87% capacity retention after the first stable cycle (5th cycle), an average drop of 0.067% per cycle. The Coulombic efficiency kept around 98% and slowly dropped to 95% after 200 cycles, due to gradual consumption of the LiNO₃ additive. In contrast, because of its lower conductivity and thus lower utilization of sulfur, PSC−S showed a lower specific capacity at this high current rate. The charge−discharge profiles of PSC−CNT−S at various current densities were shown in Figure 5c. As current density ramps up, both discharge capacity and output voltage showed a mild decrease. However, due to the high conductivity of the material, neither capacity nor voltage profile was severely affected.

3. CONCLUSION

Microsized spherical carbon−sulfur composites were designed to reach high tap density and high sulfur content and to fabricate electrodes with high sulfur loading, with an eye toward practical applications of Li−S batteries. Both microspherical particle morphology and hierarchical mesoporous structure with high surface area and pore volume of the carbon frameworks were well controlled by a combination of EISA and emulsion polymerization. The carbon−sulfur composites had a high tap density of ∼1 g/mL and were shown to have solid performance as Li−S cathodes despite the high electrode-level sulfur content of 60 wt % and high sulfur loading of 5 mg S/cm² in electrodes. In addition, the incorporation of CNTs into the microspherical particles was found to decrease resistance of the composite and allow for improved high-current-density performance. This highly scalable synthesis approach shows a promising direction for future designs of C−S composites as Li−S cathode materials for practical applications.

■ EXPERIMENTAL SECTION

Materials. Block copolymer F127 (M_w = 12 600, PEO₁₀₆PPO₇₀PEO₁₀₆), tetraethyl orthosilicate (TEOS, 99%), Span 80 (viscosity 1200−2000 mPa s at 20 °C), and multiwalled carbon nanotube (CNT, OD*L, 6−9 nm × 5 μm) were purchased from Sigma-Aldrich. Ethanol (>99.8%), hydrochloric acid (HCl, 36.5%), hydrofluoric acid (HF, 48−51%), carbon disulfide (CS₂, 99.8%), and Triton X-100 were purchased from Alfa Aesar. Paraffin oil (light) was purchased from EMB Millipore. Colloidal silica latex SNOWTEX ST-O (10−20 nm, 20 wt %) was gifted by Nissan Chemical America Corporation. The resin precursor (M_w < 500) was prepared according to the literature method.[29]

Synthesis of PSC Microspheres. In a typical preparation of PSC, 3.3 g of F127 was first dissolved in 20 g of ethanol with 2.0 g of HCl (0.2 M). Then, 4.16 g of TEOS was added, and the clear solution was stirred for 0.5 h at 40 °C. Next, 11 g of resin solution (20 wt %) and 12 mL of colloidal silica ST-0 were added in sequence and further stirred for 1 h. Meanwhile, 3 g of emulsifier, Span80, was dispersed in a 300 mL paraffin oil bath at 40 °C. The ethanol solution was added into the oil bath for emulsification by vigorous stirring. The temperature was kept at 40 °C for 1 h and tuned to 100 °C to evaporate ethanol and thermopolymerize overnight. The as-made products were filtered and washed with hexane several times before drying in air. Calcination was carried out sequentially in a tubular furnace, first at 350 °C for 3 h and next at 900 °C for 2 h under Ar flow to get the PSC−SiO₂

nanocomposite. The heating rate was 1 °C/min below 600 °C and 5 °C/min above 600 °C. The PSC−SiO₂ nanocomposite was immersed in 2 wt % HF solutions to remove silica, leaving PSC carbon spheres. The as-made product was washed by distilled water several times and dried at 80 °C in an oven.

Synthesis of PSC−CNT Microspheres. PSC−CNT was synthesized similarly. An amount of 100 mg of CNTs was dispersed in 10 mL ethanol with the assitance of Triton X-100 and sonication. This suspension was added to the ethanol solution of resin, F127, TOES, ST-0, and HCl and stirred for 0.5 h before being emulsified in the paraffin oil bath.

Synthesis of PSC−S and PSC−CNT−S Composites. To synthesize the PSC−S and PSC−CNT−S composites, 750 mg of sulfur was first dissolved in CS₂ by stirring. An amount of 250 mg of PSC or PSC−CNT was then added to the solution and allowed CS₂ evaporation under stirring. The mixture was then transferred into a closed bottle and heated at 155 °C for 8 h to yield the sulfur-embedded composites.

Electrochemical Measurement. The electrochemical experiments were performed using 2016-type coin cells, which were assembled in an argon-filled dry glovebox (MBraun, Inc.) with the PSC−S, PSC−CNT−S, and Super P−S electrodes as the working electrode and the Li metal as the counter electrode. The PSC−S and PSC−CNT−S electrodes were prepared by casting the slurry consisting of 80 wt % of either carbon−sulfur composite, 12 wt % of SuperP carbon black, and 8 wt % of polyvinylidene fluoride (PVDF) binder. The SuperP−S electrodes were prepared by casting the slurry consisting of 92 wt % of sulfur/SuperP ball-milled mixture and 8 wt % of polyvinylidene fluoride (PVDF) binder, where the sulfur−SuperP mixture was ball milled overnight at a speed of 500 rpm. All electrodes have a loading of 5.0 mg S/cm² (±5%) by controlling the area of coating. 1 M LiTFSI and 0.2 M LiNO₃ in a mixture of 1,3-dioxanes and dimethoxyethane (DOL:DME, 1:1 by vol. %) was used as the electrolyte (Novolyte Technologies, Independence, OH). The electrochemical performance was evaluated by galvanostatic charge/discharge cycling on an Arbin BT-2000 battery tester at room temperature under different current densities in the voltage range between 1.7 and 2.8 V versus Li⁺/Li. The specific capacity is calculated based on the mass of sulfur.

Characterization. The crystalline structure of the as-prepared composite was characterized by X-ray diffraction (XRD) on a Rigaku Miniflex II spectrometer. The microstructure of the composite particles was investigated with a JEOL 1200 transmission electron microscope (TEM). Scanning electron microscope (SEM) images and energy-dispersive X-ray spectroscopy (EDX) elemental mapping were taken on a NanoSEM 630. The surface area and pore structure were characterized by nitrogen sorption using a Micrometrics ASAP 2020 physisorption analyzer. The surface area was calculated by the Brunauer−Emmett−Teller (BET) method. The pore size distributions were derived from the adsorption branches of isotherms using the Barrett−Joyner−Halenda (BJH) model. The content of sulfur in the composites was characterized by thermogravimetric analysis (TGA) in the temperature range of 25−600 °C with a heating rate of 10 °C/min under nitrogen atmosphere. Dynamic light scattering (DLS) experiments were performed on a Malvin Mastersizer. Electrical resistivity of powder materials was measured by compressing the powder in a cylindrical space and getting its resistance, which is then converted to conductivity and resistivity using the geometrical parameters of the cylindrical space.[39,40] The pressure among powder particles can be controlled with the force of compression. Tap density of materials was determined by calculating the ratio of the mass of the measured material to its tapped volume. A certain amount of the measured material was tapped in a vial 100 times before its tapped volume was measured.

■ ASSOCIATED CONTENT

Ⓢ Supporting Information

Calculation for required sulfur loading, SEM images, TGA results, N₂ sorption isotherms, X-ray diffraction patterns, and

photo images of electrodes are included. This material is available free of charge via the Internet at http://pubs.acs.org.

■ AUTHOR INFORMATION

Corresponding Author
*E-mail: dwang@psu.edu.

Author Contributions
‡These authors contributed equally.

Notes
The authors declare no competing financial interest.

■ REFERENCES

(1) Bruce, P. G.; Freunberger, S. A.; Hardwick, L. J.; Tarascon, J. M. *Nat. Mater.* **2012**, *11*, 19−29.
(2) Ji, X.; Nazar, L. F. *J. Mater. Chem.* **2010**, *20*, 9821−9826.
(3) Nelson, J.; Misra, S.; Yang, Y.; Jackson, A.; Liu, Y.; Wang, H.; Dai, H.; Andrews, J. C.; Cui, Y.; Toney, M. F. *J. Am. Chem. Soc.* **2012**, *134*, 6337−6343.
(4) Cheon, S. E.; Ko, K. S.; Cho, J. H.; Kim, S. W.; Chin, E. Y.; Kim, H. T. *J. Electrochem. Soc.* **2003**, *150*, A796−A799.
(5) Barchasz, C.; Molton, F.; Duboc, C.; Leprêtre, J. C.; Patoux, S.; Alloin, F. *Anal. Chem.* **2012**, *84*, 3973−3980.
(6) Diao, Y.; Xie, K.; Xiong, S.; Hong, X. *J. Power Sources* **2013**, *235*, 181−186.
(7) Cañas, N. A.; Wolf, S.; Wagner, N.; Friedrich, K. A. *J. Power Sources* **2013**, *226*, 313−319.
(8) Diao, Y.; Xie, K.; Xiong, S.; Hong, X. *J. Electrochem. Soc.* **2012**, *159*, A421−A425.
(9) Mikhaylik, Y. V; Akridge, J. R. *J. Electrochem. Soc.* **2004**, *151*, A1969−A1976.
(10) Liang, C.; Dudney, N. J.; Howe, J. Y. *Chem. Mater.* **2009**, *21*, 4724−4730.
(11) Ji, X.; Lee, K. T.; Nazar, L. F. *Nat. Mater.* **2009**, *8*, 500−506.
(12) Fu, Y.; Su, Y. S.; Manthiram, A. *ACS Appl. Mater. Interfaces* **2012**, *4*, 6046−6052.
(13) Xin, S.; Gu, L.; Zhao, N. H.; Yin, Y. X.; Zhou, L. J.; Guo, Y. G.; Wan, L. *J. Am. Chem. Soc.* **2012**, *134*, 18510−18513.
(14) Chen, S. R.; Dai, F.; Gordin, M. L.; Wang, D. H. *RSC Adv.* **2013**, *3*, 3540−3543.
(15) Song, J. X.; Xu, T.; Gordin, M. L.; Zhu, P. Y.; Lv, D. P.; Jiang, Y-B; Chen, Y. S.; Duan, Y. H.; Wang, D. H. *Adv. Funct. Mater.* **2013**, DOI: 10.1002/adfm.201302631.
(16) Chen, Z.; Dahn, J. R. *J. Electrochem. Soc.* **2002**, *149*, A1184−A1189.
(17) Cheon, S. E.; Ko, K. S.; Cho, J. H.; Kim, S. W.; Chin, E. Y.; Kim, H. T. *J. Electrochem. Soc.* **2003**, *150*, A800−A805.
(18) Zheng, H.; Li, J.; Song, X.; Liu, G.; Battaglia, V. S. *Electrochim. Acta* **2012**, *71*, 258−265.
(19) Bae, C. J.; Erdonmez, C. K.; Halloran, J. W.; Chiang, Y. M. *Adv. Mater.* **2013**, *25*, 1254−1258.
(20) Zhang, S. S. *J. Power Sources* **2013**, *231*, 153−162.
(21) Seh, Z. W.; Li, W.; Cha, J. J.; Zheng, G.; Yang, Y.; McDowell, M. T.; Hsu, P. C.; Cui, Y. *Nat. Commun.* **2013**, *4*, 1331.
(22) Schuster, J.; He, G.; Mandlmeier, B.; Yim, T.; Lee, K. T.; Bein, T.; Nazar, L. F. *Angew. Chem., Int. Ed.* **2012**, *51*, 3591−3595.
(23) Wang, H.; Yang, Y.; Liang, Y.; Robinson, J. T.; Li, Y.; Jackson, A.; Cui, Y.; Dai, H. *Nano Lett.* **2011**, *11*, 2644−2647.
(24) Lee, Y. M.; Choi, N. S.; Park, J. H.; Park, J. K. *J. Power Sources* **2003**, *119*, 964−972.
(25) Yang, Y.; Yu, G.; Cha, J.; Wu, H. *ACS Nano* **2011**, *5*, 9187−9193.
(26) Harkins, W. D. *J. Am. Chem. Soc.* **1947**, *69*, 1428−1444.
(27) Brinker, C. J.; Lu, Y. F.; Sellinger, A.; Fan, H. Y. *Adv. Mater.* **1999**, *11*, 579−585.
(28) Gu, D.; Bongard, H.; Deng, Y.; Feng, D.; Wu, Z.; Fang, Y.; Mao, J.; Tu, B.; Schüth, F.; Zhao, D. *Adv. Mater.* **2010**, *22*, 833−837.
(29) Liu, R.; Shi, Y.; Wan, Y.; Meng, Y.; Zhang, F.; Gu, D.; Chen, Z.; Tu, B.; Zhao, D. *J. Am. Chem. Soc.* **2006**, *128*, 11652−11662.
(30) Cao, Y.; Li, X.; Aksay, I. A; Lemmon, J.; Nie, Z.; Yang, Z.; Liu, J. *Phys. Chem. Chem. Phys.* **2011**, *13*, 7660−7665.
(31) Scott, G. D.; Kilgour, D. M. *J. Phys. D: Appl. Phys.* **1969**, *2*, 863−866.
(32) Applestone, D.; Manthiram, A. *RSC Adv.* **2012**, *2*, 5411−5417.
(33) Yi, R.; Dai, F.; Gordin, M. L.; Chen, S.; Wang, D. *Adv. Energy Mater.* **2012**, *3*, 295−300.
(34) Su, Y. S.; Manthiram, A. *Chem. Commun.* **2012**, *48*, 8817−8819.
(35) Jayaprakash, N.; Shen, J.; Moganty, S. S.; Corona, A.; Archer, L. A. *Angew. Chem., Int. Ed.* **2011**, *123*, 6026−6030.
(36) Hagen, M.; Dörfler, S.; Fanz, P.; Berger, T.; Speck, R.; Tübke, J.; Althues, H.; Hoffmann, M. J.; Scherr, C.; Kaskel, S. *J. Power Sources* **2013**, *224*, 260−268.
(37) Yabuuchi, N.; Ohzuku, T. *J. Power Sources* **2003**, *119*, 171−174.
(38) Taberna, P. L.; Mitra, S.; Poizot, P.; Simon, P.; Tarascon, J. M. *Nat. Mater.* **2006**, *5*, 567−573.
(39) Pantea, D.; Darmstadt, H.; Kaliaguine, S.; Summchen, L.; Roy, C. *Carbon* **2001**, *39*, 1147−1158.
(40) Pantea, D.; Darmstadt, H.; Kaliaguine, S.; Roy, C. *Appl. Surf. Sci.* **2003**, *217*, 181−193.

11362

dx.doi.org/10.1021/am4035784 | *ACS Appl. Mater. Interfaces* 2013, 5, 11355−11362